Electronic Supplementary Material (ESI) for Journal of Materials Chemistry A.

Electronic Supporting Information

Facilitating reversible transition metal migration and expediting ion diffusivity via oxygen vacancy for high performance O3-type layered oxide cathodes

Chenhan Lin, Xiangcong Meng, Min Liang, Wenya Li, Jinji Liang, Tengfei Liu, Xi Ke, Jun Liu, Zhicong Shi and Liying Liu*

School of Materials and Energy, Guangzhou Key Laboratory of Low-dimensional Materials and Energy Storage Devices, Guangdong University of Technology, Guangzhou 510006, China
*Corresponding author
Email: liyingliusy@gdut.edu.cn (Liying Liu).

Material preparation of OV-NCO

OV-NCO materials were synthesized via a hydrogen reduction assisted by spray-drying method. Typically, 20 g sodium chromate tetrahydrate ($Na_2CrO_4 \cdot 4H_2O$, 99.0%, Aladdin) was first dissolved in 800 mL deionized water, and then stirred constantly at room temperature for 1h. Next, the above solution was spray-dried using a NAI-GZJ Mini Spray Dryer to obtain the anhydrous sodium chromate precursor. The detailed conditions during spray drying were listed as follows: inlet temperature 260 ℃, inside diameter setting 3 mm and feeding speed 320 mL h^{-1}. After that, the yellow precursors were sintered at 850 ℃ for 6 h in an Ar/H_2 (95:5, vol %) atmosphere. The green powders (OV-NCO) in the reduced products, located in the central area of alumina crucible, were selectively collected and grounded and then rapidly transferred into an Ar-filled glove box to avoid contamination with moisture. The rest white $NaAlO_2$ powder (see **Figure S1**) stuck on the crucible wall, originated from the chemical reaction of NaOH and alumina crucible at high temperature, should be completely discarded. The detailed synthesis process of S-NCO is described in the Supporting Information.

Material preparation of S-NCO

First, a stoichiometric amount of sodium acetate anhydrous (CH_3COONa, 99.0%, Aladdin) (5 wt% excess) and chromic acetate (CH_3COOCr, 99.9%, Aladdin) were first dissolved in 800 mL deionized water, and then stirred constantly at room temperature for 1 h. Next, the solution was spray-dried using a NAI-GZJ Mini Spray Dryer to obtain the anhydrous green precursors. The detailed conditions during spray drying were same as those of OV-NCO. After that, the precursors were preheated at 450 ℃ for 2 h with a ramping rate of 1 ℃ min^{-1} in a muffle furnace. After cooling down to room temperature, the residual was grounded and sintered at 900 ℃ for 10 h with a ramping rate of 2 ℃ min^{-1} in an Ar/H_2 (95:5, vol %) atmosphere. After cooling down to around 200 ℃, the as-prepared S-NCO sample was transferred into a

glovebox immediately.

Materials characterization

A Bruker D8 Advance X-ray diffractometer with Cu Kα radiation was used to investigate the crystallographic structure of the samples. The elemental proportion was tested by ICP-OES (iCAP 7000, ThermoFisher Scientific Inc.). The morphology and elemental distribution were characterized by SEM using a field-emission scanning electron microscope (SU8220, Hitachi Ltd.) equipped with EDS. A transmission electron microscope (FEI Tecnai G^2 F30, ThermoFisher Scientific Inc.) operating at an accelerating voltage of 300 kV in combination with EELS was implemented for the analysis of surface structure and chemistry. EPR was carried out using an EMXplus-10/12 (Bruker) spectrometer with a microwave frequency of 9.84 GHz and modulation amplitude of 4.00 G. Chemical valence sate analysis was conducted on an X-ray photoelectron spectrometer (Escalab 250Xi, ThermoFisher Scientific Inc.) using monochromated Al Kα radiation. The acquired spectra were calibrated with 284.8 eV of C 1s for high-resolution scans.

Electrochemical measurements

A slurry was prepared by blending the active material, acetylene black (Canrd Ltd.) and poly (vinylidene fluoride) binder (PVDF, Canrd Ltd.) with a weight ratio of 80:10:10, applying N-methyl-2-pyrrolidone (NMP) for solvent. After mixing homogenously, the slurry was doctor-bladed on Al foil and dried at 120 ℃ in a vacuum oven. The typical CR2032-type coin half-cells were assembled in an argon-filled glove box (H_2O and O_2 content lower than 0.1 ppm), selecting Na metal foil as the counter electrode and glass microfiber (Whatman GF/D Ltd.) as the separator. 1 M $NaClO_4$ in a mixture of ethylene carbonate (EC) and propylene carbonate (PC) (mixing ratio EC/PC = 1:1 (vol%)) with 5 vol% fluoroethylene carbonate (FEC) was chosen as the electrolyte. The coin-type cells were cycled using a LAND CT2001A battery testing

system (LAND Electronics Ltd., China). GITT and EIS measurements were performed on an electrochemical workstation (Chenhua Ltd). EIS was conducted before and after cycles with a perturbation voltage of 10 mV in the frequency range of 0.0001 Hz–100 kHz. GITT measurements were employed with the test protocol consisting of 10 min charge/discharge at a current rate of 0.1C and relaxation periods of 1 h.

For the Na||OV-NCO pouch cells assembly, the size of OV-NCO cathode on the Al foil current collector was controlled as 2.5×3 cm^2. The Na metal was cut into a rectangle of 3×4 cm^2, and then pressed on the Cu foil current collector as anode. Aluminum-plastic pouch were attached on both electrodes and the pouch cell stack was assembled inside the argon-filled glove-box with the separator of glass microfiber and the electrolyte of the $NaClO_4$ solution (1 M) in EC/ PC (1:1, vol) with 5% FEC. The electrochemical tests of pouch cells were conducted with the BT-2018C battery testing system (LANBO Ltd.).

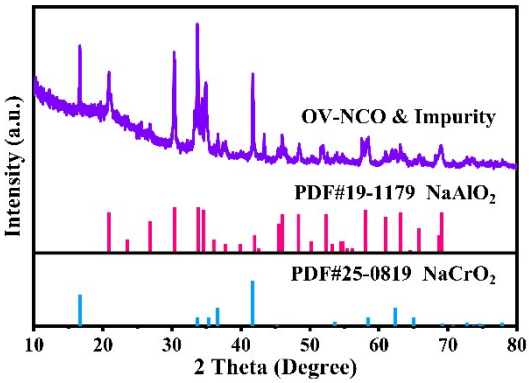

Figure S1. XRD pattern of $NaAlO_2$ impurity mixed with OV-NCO.

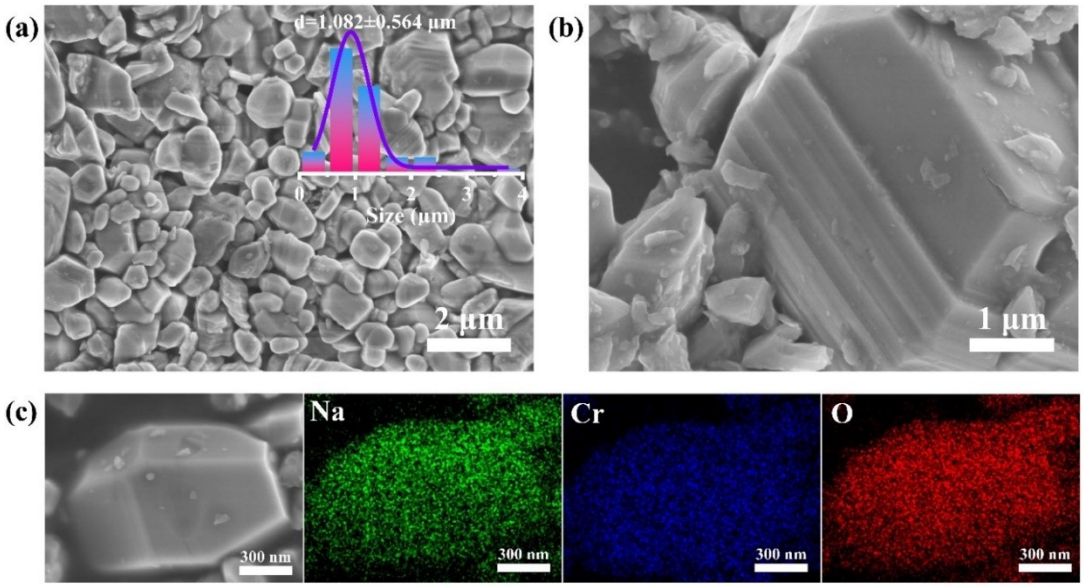

Figure S2. Morphological characterization and element distribution of OV-NCO. (a) SEM image (inset of particle size distribution histogram). (b) selected area SEM image. (c) EDS mapping images of Na, Cr, and O.

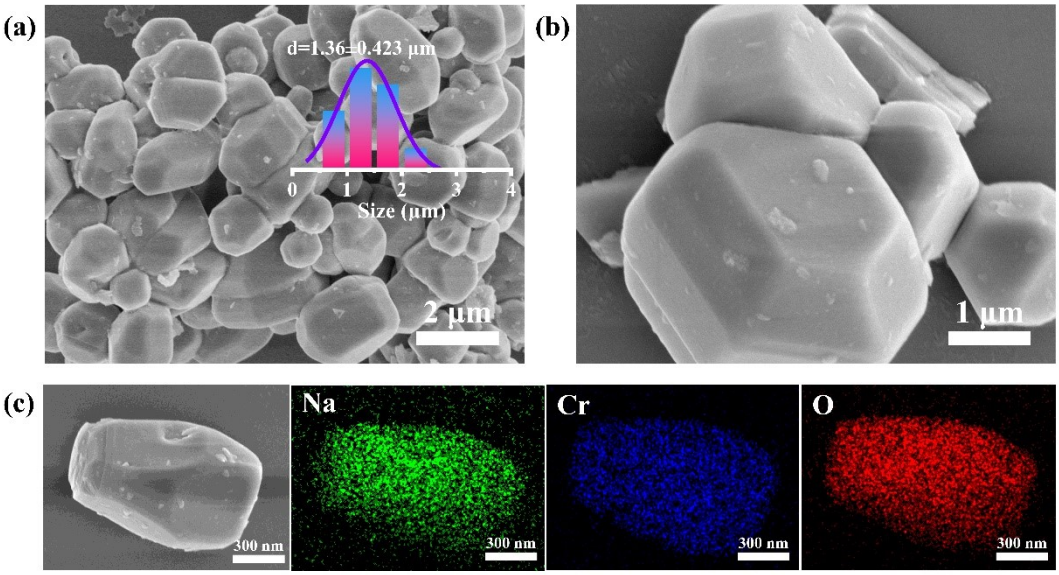

Figure S3. Morphological characterization and element distribution of S-NCO. (a) SEM image (inset of particle size distribution histogram). (b) selected area SEM image. (c) EDS mapping images of Na, Cr, and O.

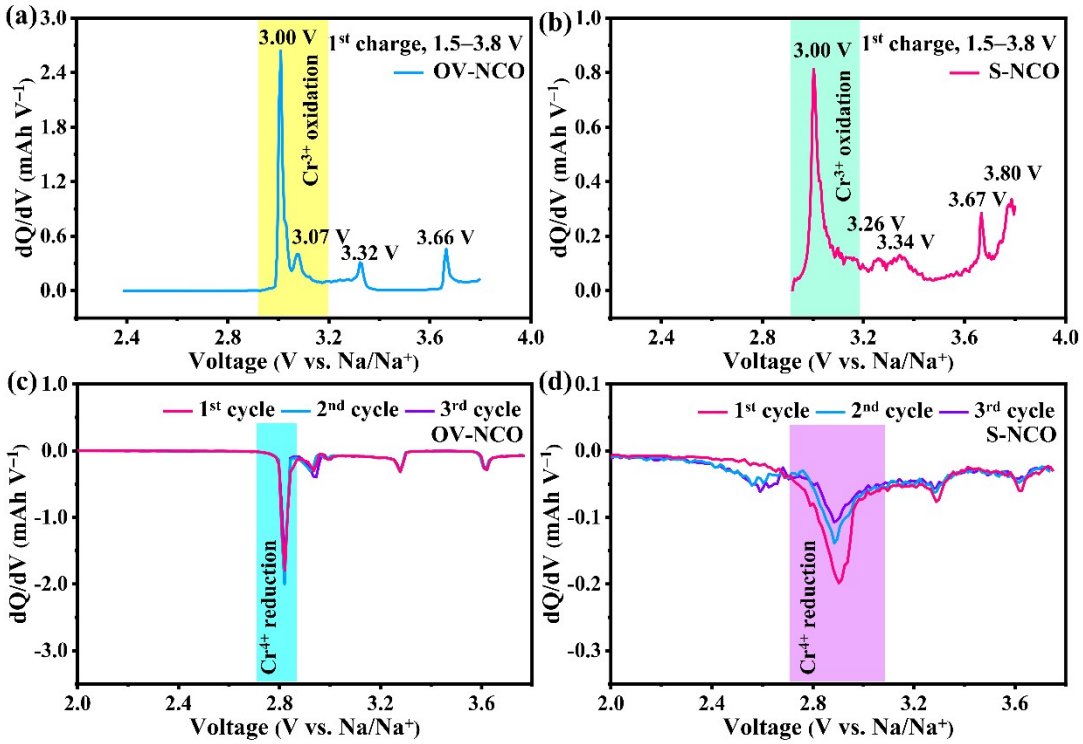

Figure S4. Charged d*Q*/d*V* vs. voltage curves of (a) OV-NCO and (b) S-NCO at the first cycle. Discharged d*Q*/d*V* vs. voltage curves for the initial three cycles of (c) OV-NCO and (d) S-NCO.

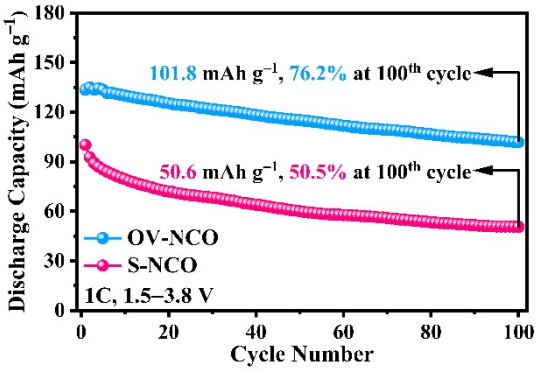

Figure S5. Comparison of cycling performance of OV-NCO and S-NCO in the voltage range of 1.5-3.8 V at 1C.

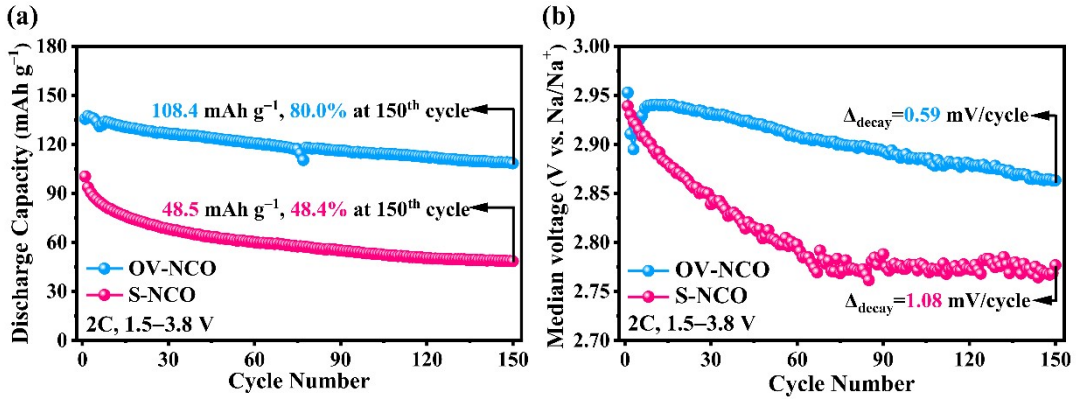

Figure S6. (a) Comparison of cycling performance of OV-NCO and S-NCO in the voltage range of 1.5-3.8 V at 2C and (b) corresponding median discharge voltage fading curves.

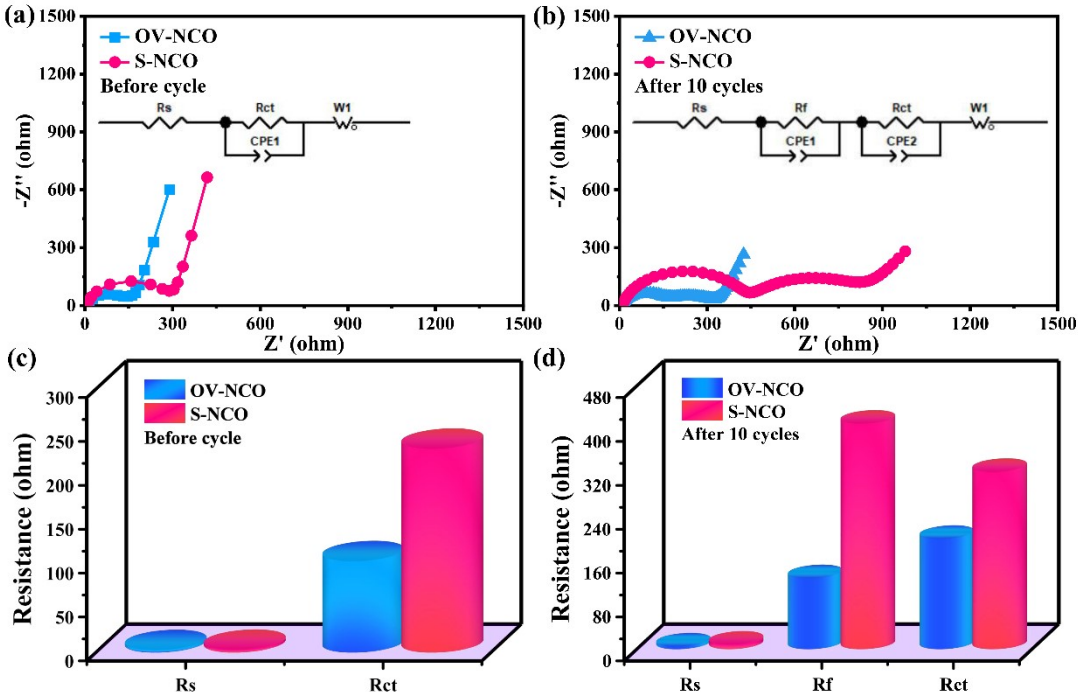

Figure S7. Nyquist plots of OV-NCO and S-NCO (a) before cycle and (b) after 10 cycles; (c, d) estimated R_s, R_f, and R_{ct} values extracted from the plots (a, b) using the equivalent circuit.

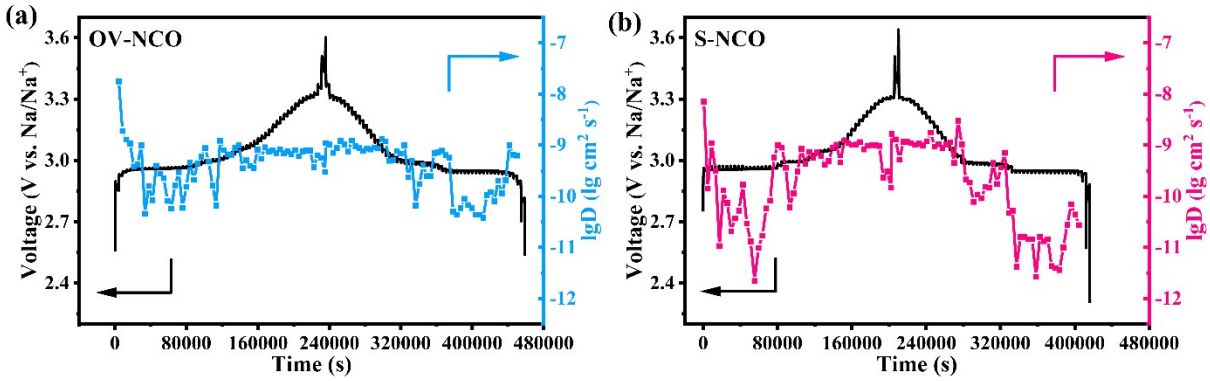

Figure S8. The first charge/discharge profiles of (a) OV-NCO and (b) S-NCO in the voltage range of 2.3-3.6 V for GITT tests with corresponding Na^+ diffusivity coefficients.

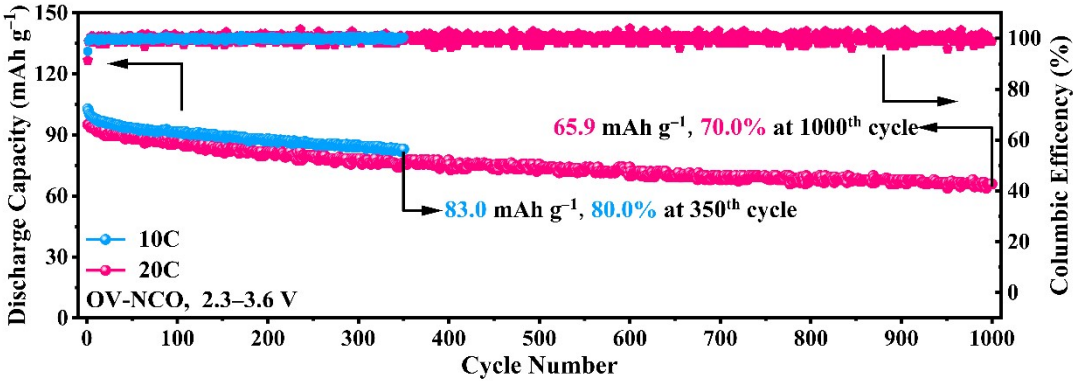

Figure S9. Long-term cyclic performance of OV-NCO in the voltage range of 2.3-3.6 V at 10C and 20C.

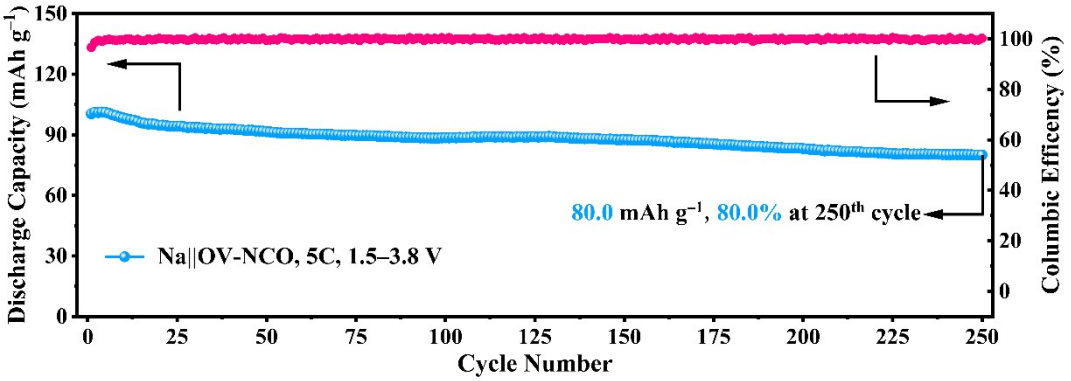

Figure S10. Cyclic performance of Na||OV-NCO pouch cells in the voltage range of 1.5-3.8 V at 5C.

Table S1. Structure parameters for OV-NCO as determined by Rietveld refinement of powder XRD data at room temperature[#].

Element	x	y	z	Occupancy
Na	3	0	0	0.99989
Cr	3	0	0	1.00003
O	6	0	0	0.95228

a=b=2.97021 Å, c=15.9398 Å (c/a=5.37); α=β=90°, γ=120°.

Table S2. Structure parameters for S-NCO as determined by Rietveld refinement of powder XRD data at room temperature[#].

Element	x	y	z	Occupancy
Na	3	0	0	1.00000
Cr	3	0	0	1.00000
O	6	0	0	0.99989

a=b=2.97021 Å, c=15.9334 Å (c/a=5.36); α=β=90°, γ=120°.

Table S3. ICP-OES results of OV-NCO and S-NCO

Samples	Theoretical ratio	Experimental ratio
	Na:Cr	Na:Cr
OV-NCO	1:1	0.9904:1
S-NCO		0.9596:1

Table S4. Comparison of rate performances among OV-NCO and other related Cr-based layered oxide cathodes (Charge cut-off voltage beyond 3.6 V)

Cr-based layered oxide cathodes	Voltage range (V vs. Na^+ /Na)	Discharge capacities (mAh g^{-1})	Refs.
OV-NCO ($NaCrO_{2-x}$)	1.5-3.8	59.6 (100C) / 89.6 (50C)	This work
$Na_{0.95}CrO_2$	2.0-4.0	42.0 (5C)	1
$Na_{0.6}Cr_{0.6}Ti_{0.4}O_2$	2.5-3.85	48.0 (12C)	2
$Na_{0.72}Cr_{0.86}Sb_{0.14}O_2$	1.5-4.1	37.0 (30C)	3
$Na_{0.88}Cr_{0.88}Ru_{0.12}O_2$	1.5-3.8	83.6 (50C)	4
$Na_{0.9}Ca_{0.035}Cr_{0.97}Ti_{0.03}O_2$	1.5-3.8	51.6 (100C)	5

Table S5. Comparison of rate performances among bulk $NaCrO_2$ cathodes (including OV-NCO) (Charge cut-off voltage of 3.6 V or below) and other well-studied cathodes at room temperature (25 ℃)

Samples	Voltage range (V vs. Na^+ /Na)	Discharge capacities (mAh g^{-1})	Refs.
OV-NCO ($NaCrO_{2-x}$)	2.3-3.6	59.6 (140C) / 73.7 (100C)	This work
$NaCrO_2$	2.5-3.5	63.0 (20C)	6
$NaCrO_2$ nanowires	2.0-3.6	78.5 (80C)	7
Large-grained $NaCrO_2$	2.3-3.6	51.0 (30C)	8
$Na_2Fe_{0.95}V_{0.05}PO_4F$	2.0-4.0	71.6 (20C)	9
$Na_3V_2(PO_4)_3$@C	2.0-4.3	64.6 (5C)	10
$LiNi_{0.85}Co_{0.12}Al_{0.03}O_2$	2.8-4.3	82.0 (2C)	11
$LiNi_{0.8}Co_{0.1}Mn_{0.1}O_2$	2.7-4.5	23.0 (50C)	12

Table S6. Comparison of rate performances among bulk $NaCrO_2$ cathodes (including OV-NCO) (Charge cut-off voltage of 3.6 V or below) and other well-studied cathodes at elevated temperature (50-60 ℃).

Samples	Voltage range (V vs. Na^+ /Na)	Discharge capacity (mAh g^{-1})	Refs.
OV-NCO ($NaCrO_{2-x}$)	2.3-3.6	55.2 (100C)	This work
$NaCrO_2$ nanowires	2.0-3.6	36.5 (50C)	7
Large-grained $NaCrO_2$	2.3-3.6	32.0 (60C)	8
$Na_2Fe_{0.95}V_{0.05}PO_4F$	2.0-4.0	62.0 (20C)	9
$Na_3V_2(PO_4)_2F_3$	2.0-4.3	53.8 (20C)	10
$LiNi_{0.85}Co_{0.12}Al_{0.03}O_2$	2.8-4.3	82.0 (2C)	11
$LiNi_{0.8}Co_{0.1}Mn_{0.1}O_2$	2.7-4.5	23.0 (50C)	12

References

1 K. Mathiyalagan, A. Ponnaiah, K. Karuppiah, S. Rengapillai and S. Marimuthu, *Ionics*, 2020, **26**, 3929-3936.

2 Y. Wang, R. Xiao, Y.-S. Hu, M. Avdeev and L. Chen, *Nat. Commun.*, 2015, **6**, 6954.

3 W. Ko, M.-K. Cho, J. Kang, H. Park, J. Ahn, Y. Lee, S. Lee, S. Lee, K. Lee, J. Hong, J.-K. Yoo and J. Kim, *Energy Storage Mater.*, 2022, **46**, 289-299.

4 K. Y. Xi, S. F. Chu, X. Y. Zhang, X. P. Zhang, H. Y. Zhang, H. Xu, J. J. Bian, T. C. Fang, S. H. Guo, P. Liu, M. W. Chen and H. S. Zhou, *Nano Energy*, 2020, **67**, 104215.

5 I. Lee, G. Oh, S. Lee, T.-Y. Yu, M. H. Alfaruqi, V. Mathew, B. Sambandam, Y.-K. Sun, J.-Y. Hwang and J. Kim, *Energy Storage Mater.*, 2021, **41**, 183-195.

6 C. Y. Chen, K. Matsumoto, T. Nohira, R. Hagiwara, A. Fukunaga, S. Sakai, K. Nitta and S. Inazawa, *J. Power Sources*, 2013, **237**, 52-57.

7 L. W. Liang, X. Sun, D. K. Denis, J. Y. Zhang, L. R. Hou, Y. Liu and C. Z. Yuan, *Acs Appl. Mater. Interfaces*, 2019, **11**, 4037-4046.

8 Y. Wang, W. Li, G. Hu, Z. Peng, Y. Cao, H. Gao, K. Du and J. B. Goodenough, *Chem. Mater.*, 2019, **31**, 5214-5223.

9 J. M. Dong, J. C. Xiao, Y. F. Yu, J. R. Wang, F. Chen, S. Wang, L. M. Zhang, N. Q. Ren, B. C. Pan and C. H. Chen, *Energy Storage Mater.*, 2022, **45**, 851-860.

10 J. Hwang, K. Matsumoto and R. Hagiwara, *Adv. Energy Mater.*, 2020, **10**, 2001880.

11 E. Lee, W. Lee, J. Kima, H. Kima, M. Kima, S. Yun, S. Leeb, J. Kimc, D. Park, D. Kim and W. S. Yoona, *Energy Storage Mater.*, 2022, **46**, 259-268.

12 X. Y. Zhang, J. Xu, X. T. Liu, F. Y. Cheng, P. Wei, Y. Xu, S. X. Sun, H. Lin, Y. Shen, Q. Li, C. Fang and J. T. Han, *Energy Storage Mater.*, 2022, **47**, 87-97.